

Preparation of graphene-based catalysts and combined DBD reactor for VOC_S degradation

zongyang liu

Sichuan University - Wangjiang Campus: Sichuan University

yifan wang

Chengdu University of Information Technology

gengmeng zhang

Sinopec Group

jie yang

Chengdu University of Information Technology

shengyu liu (✉ shengyuliu_cuit@163.com)

Chengdu University of Information Technology

Research Article

Keywords: DDBD, Graphene, Transition metal catalysts, Benzene series, By-products

Posted Date: February 11th, 2022

DOI: <https://doi.org/10.21203/rs.3.rs-1299655/v1>

License:   This work is licensed under a Creative Commons Attribution 4.0 International License.

[Read Full License](#)

Version of Record: A version of this preprint was published at Environmental Science and Pollution Research on March 5th, 2022. See the published version at <https://doi.org/10.1007/s11356-022-19483-6>.

Abstract

The objective of this study was to compare the transformation of by-products between single dielectric barrier discharge (SDBD) and double dielectric barrier discharge (DDBD), to optimize the preparation of graphene-based catalysts and apply them in combination with DBD for VOCs degradation. The effect of three experimental conditions (initial concentration, output voltage, flow rate) on degradation rate, by-product transformation, and mineralization was investigated comparatively for SDBD and DDBD. Graphene oxide was prepared using the improved Hummers' method, and the optimal pathway of adding KMnO_4 was selected. Graphene-based catalysts were synthesized using the ion-assisted hydrothermal method. The effect of the amount of 1-butyl-3-methylimidazolium hexafluorophosphate ([BMIM]PF₆) on the preparation of three typical transition metal catalysts (Mn, Fe, and Ti) was studied. It was found that NO_2 transformation rate of DDBD was higher than that of SDBD. The addition amount and interval time of KMnO_4 affect the preparation of graphene oxide. [BMIM]PF₆ dose of 0.25 ml, the preparation of three catalysts showed the best performance. MnO_x/rGO exhibited superior performance in the degradation of benzene series, NO transformation, NO_2 transformation, CO_2 selectivity, and energy efficiency. FeO_x/rGO exhibited superior performance for O_3 transformation. Mn_3O_4 and Fe_3O_4 played a leading role in promoting the degradation of the benzene series and the transformation of by-products.

1 Introduction

Volatile organic compounds (VOCs) include non-methane hydrocarbons, oxygenated volatile organic compounds, and organochlorine compounds (Park et al., 2013). The emissions of these substances to natural environments harm human health and the ecological environment (Ehn et al., 2014). In most parts of China, the emissions of VOCs are dominated by aromatic hydrocarbons, which are high in concentration and difficult to be removed (An et al., 2014; Li et al., 2018; Fang et al., 2018; Zhu and Liu., 2014; Luo et al., 2020). Benzene series chemicals such as benzene and toluene are the main harmful substances for human body and the environment (Ran et al., 2018; Zhang et al., 2017). Low-temperature plasma technology can rapidly degrade VOCs and has a wide range of applications. Dielectric barrier discharge (DBD) technology makes the discharge evenly distributed on the surface of the dielectric through extreme insertion of high voltage (Yu et al., 2019). Based upon the structure, DBD is classified as single dielectric barrier discharge (SDBD) and double dielectric barrier discharge (DDBD). Liang et al. (2015) used toluene as a typical VOC and DBD technology to study its peak voltage, gas flow, initial toluene concentration, discharge frequency, and working cycle. Mustafa et al. (2018) studied the relationship between medium spacing and degradation efficiency in an experimental study using DDBD. Zhang et al. (2014) studied and optimized various parameters such as applied voltage and discharge length by comparing the performance of SDBD and DDBD in degrading styrene, and detected and discussed the by-products of O_3 and NO_x .

Increasing the DBD energy can improve the removal efficiency of VOCs, which is inconsistent with the principles of energy-savings and removal efficiency, and can produce harmful by-products (such as O_3

and NO_x). In order to cover the shortages of low-temperature plasma technology, the catalytic technology, which can further enhance the removal efficiency and reduce by-products, is combined with the low-temperature plasma technology (Yao et al., 2018, 2019). Transition metals are often used as catalytic materials for synergistic low-temperature plasma due to their low cost and high performance. Yao et al. (2019) studied the degradation of toluene using NB-Mn/McM-41 in a DBD reactor and confirmed that the metal was highly dispersed on the surface of McM-41. Huang et al. (2011) studied how to improve the removal efficiency of mixed VOCs and control by-products in the emission process. According to different types of pollutants, the coordination between the transition metal catalyst types and DBD is also different (Herrera et al., 2019; Alqahtani et al., 2020). The supporting materials can improve the catalytic performance, reduce the amount of catalyst required, increase the catalytic activity, and include materials such as activated carbon, molecular sieves, and graphene. Graphene is an emerging material, and has a huge specific surface area and strong plasticity and ductility, which can solve the problems of agglomeration and low activity in catalyst loading. The preparation methods of graphene oxide (GO) and reduced graphene oxide (rGO) composite catalysts include oxidation reduction method, vapor deposition method, blending method, and hydrothermal method (Tseng et al., 2010; Mishra et al., 2013; Hao and Ji., 2012; Yukimura et al., 2005). Lian et al. synthesized GO and rGO using an improved Hummers' method (IHM). The method can effectively produce GO and reduce GO from graphene. The layer spacing of the prepared GO was higher than that of rGO, and the specific surface area of rGO ($292.6 \text{ m}^2/\text{g}$) was larger than that of GO ($236.4 \text{ m}^2/\text{g}$) (Lian et al., 2017).

Since most researchers have focused on preparing catalysts and optimizing plasma, only a few studies have used graphene as a catalyst carrier for the DBD reactor. In addition, the performances of SDBD and DDBD for the degradation of benzene series and its by-products are unknown. In the present study, the optimal experimental conditions were obtained by comparing the degradation rate of benzene series, the transformation rate of by-products, energy efficiency, and other indicators. Based on IHM and different methods to add KMnO_4 , the preparation conditions of GO were optimized using cheap flake graphite (FG) as the raw material. In order to explore the performance of Mn, Fe, and Ti in the degradation of benzene series, graphene-based catalytic materials were prepared using ionic liquid-assisted hydrothermal method. The effect of the addition of ionic liquid on the catalyst was studied. The synthesized catalyst and the optimal reactor conditions were used to discuss the degradation of benzene series and the formation of by-products and CO_2 . The results from the study provide theoretical guidance for the plasma synergistic catalyst technology.

2 Experimental

2.1 Experimental setup

Figure 1 shows the combination of DBD reactor and the catalyst system. The airflow controller (Chengdu Times Hongyu Testing Instrument Co., Ltd., Chengdu, China) was used to control the initial flow. DBD (Nanjing Suman Plasma Co., Ltd., Nanjing, China) was connected to the regulator (Zhejiang Chint Electric

Appliance Co., Ltd., Hangzhou, China), and its initial voltage was adjustable. The DBD reactor was connected with the oscilloscope (UTD2102cex) to observe the variation in waveform of the reactor. The tail gas was analyzed using the O₃ detector (Zhejiang Healthyphoton Co., Ltd., Hangzhou, China) and GS-MS (Chongqing Chuanyi Ninth Factory, Chongqing, China) system. Figure 1 shows the structural differences between the SDBD and DDBD systems. The catalyst was loaded in a transparent tube with high-temperature resistance, and a dense stainless steel mesh carried the catalyst at the bottom.

2.2 Electrical parameters

The main electrical parameters were the initial voltage (IV), output voltage (OV), discharge power (DP), specific energy density (SED), and energy efficiency (EE). The oscilloscope was used to connect the two channels (CH1 and CH2) to the discharge host's IC detection port and the U detection port of the dielectric barrier device, respectively. The corresponding voltage (VM, VO) and capacitance were obtained by series measurements. Two channels were added to the oscilloscope to obtain the closed curve, whereas the discharge power was obtained according to the V-Q (Lissajous-Figure). The discharge power is calculated using Equation (1).

$$P(w) = f \int_0^t V(t) I dt = f C M \int V dV M \quad (1)$$

where P is the power (W), f is the frequency (Hz), CM is the reactor capacitance (F) and VM is the reactor voltage (V).

SED refers to the electric energy obtained when the gas enters the device (J/L), and is calculated using Equation (2).

$$SED(J/L) = \frac{P}{Q}$$

2

where P is the power (W), and Q is the airflow (L/s).

EE is an important indicator of energy consumption for treating VOCs (Ji et al., 2021), and directly reflects the energy consumption of the device. In this paper, the EE is defined as the energy consumed to remove a unit mass of VOCs (g/kWh) and is given by Equation (3).

$$EE(g/Kwh) = \frac{C_{in} - C_{out}}{SED} \times 3.6$$

3

where C_{in} is the initial gas concentration (ppm), and C_{out} is the outlet gas concentration (ppm).

2.3 Data processing

The components of VOCs were benzene and toluene. The standard curve was obtained using the chromatographic column (wax) combined with GC-MS (Chongqing Chuanyi Ninth Factory). The O₃ transformation rate is calculated using Equation (4), the NO and NO₂ transformation rate are calculated using Equation (5)-(6), the mineralization of benzene and toluene is calculated using Equation (7)-(8).

$$O_3 \text{ Transformation Rate (\%)} = \frac{c_{O_{3in}} - c_{O_{3out}}}{c_{O_{3in}}} \times 100\% \quad (4)$$

Where $c_{O_{3in}}$ is the initial O₃ concentration (ppm), and c_{out} is the outlet O₃ concentration (ppm).

$$NO \text{ Transformation Rate (\%)} = \frac{c_{NO_{in}} - c_{NO_{out}}}{c_{NO_{in}}} \times 100\% \quad (5)$$

Where $c_{O_{3in}}$ is the initial NO concentration (ppm), and c_{out} is the outlet NO concentration (ppm).

$$NO_2 \text{ Transformation Rate (\%)} = \frac{c_{NO_{2in}} - c_{NO_{2out}}}{c_{NO_{2in}}} \times 100\% \quad (6)$$

Where $c_{O_{3in}}$ is the initial NO₂ concentration (ppm), and c_{out} is the outlet NO₂ concentration (ppm).

$$\text{Mineralization(Toluene) (\%)} = \frac{c_{CO_2}}{7(c(\text{Toluene})_{in} - c(\text{Toluene})_{out})} \times 100\%$$

7

Where c_{CO_2} is the outlet CO₂ concentration (ppm), $c(\text{Toluene})_{in}$ is the inlet toluene concentration (ppm), and $c(\text{Toluene})_{out}$ is the outlet toluene concentration (ppm).

$$\text{Mineralization(Benzene) (\%)} = \frac{c_{CO_2}}{6(c(\text{Benzene})_{in} - c(\text{Benzene})_{out})} \times 100\%$$

8

Where c_{CO_2} is the outlet CO₂ concentration (ppm), $c(\text{Benzene})_{in}$ is the inlet toluene concentration (ppm), and $c(\text{Benzene})_{out}$ is the outlet toluene concentration (ppm).

2.4 Preparation of materials

2.4.1 GO preparation

The principle of IHM is that graphite is oxidized to graphite oxide by the oxidant, which is then ultrasonically exfoliated into GO with fewer layers or monolayers. First, 150 ml of concentrated H₂SO₄ and 45 ml H₃PO₄ were taken and mixed carefully and slowly. Then, 4g of FG was added to the above solution, mixed uniformly by stirring the solution. Then, 20g of KMnO₄ was taken under ice bath

conditions and slowly added to the mixture during stirring (The first solution was added with 10g KMnO_4 twice at an interval of 30 minutes. The second solution was added with 5g KMnO_4 four times with an interval of 10 minutes.). The resultant GO solutions were called GO1, and GO2. The reaction temperature was controlled at no more than 5 °C, and the ice water bath was removed after stirring for 30 min. The temperature was controlled at about 50 °C and stirred for 2 h. Bubbles were generated (brown-green thick) and slowly added to deionized water. The temperature increased to 100 °C and maintained for 15 min. The mixture was yellowish-brown. An appropriate amount of H_2O_2 (30 wt.%) was added until the solution became bright yellow. The yellowish-brown solid was obtained after hot filtration, which was washed successively with HCl (10%) solution, and distilled water until no SO_4^{2-} (BaCl_2 solution identification) was detected. The obtained yellowish-brown precipitate was the graphite oxide. To form a brown solution, an appropriate amount of deionized water was added and the mixture was ultrasonically treated for 2 h. Finally, the obtained mixed solution was centrifuged, dried at 80 °C and stored.

2.4.2 rGO-based catalyst preparation

GO solution (500 mg/L) was ultrasonically treated for 1 h and mixed with the loaded MnO_x , FeO_x , and TiO_x (manganous acetate, ferric nitrate nonahydrate, and tetrabutyl titanate; 15 wt.%) for 10 min. Then, 1-butyl-3-methylimidazolium hexafluorophosphate ([BMIM]PF₆) was quantitatively dropped into the mixed system. Moreover, 150 mg of Vitamin C was added, and pH was adjusted to 10 using concentrated ammonia. The solution was stirred for 50 min at room temperature. Subsequently, the polytetrafluoroethylene-coated vessel was immediately incorporated, and the hydrothermal reaction was carried out at 200°C for 10 h. After the reaction, it was dried in a vacuum drying oven at 60°C and stored after calcination.

2.5 Catalysts characterization

An FEI Inspect F50 (FSEM) electric field emission scanning electron microscope was used. The working voltage was set to be 10 kV. Moreover, a DX-2700 X-ray diffractometer was used for XRD analysis. The voltage was 40 kV, and the diffraction angle lied within the range of 20 - 80°. The scanning speed was 8°/min. Furthermore, 0.1 g of sample was degassed at 100°C for 1 h and then further degassed at 350°C for 4 h. After degassing, N_2 was used as adsorbate at -196°C. BET method was used to calculate the specific surface area of the sample, whereas BJH method was used to calculate the pore volume and pore size. X-ray photoelectron spectroscopy (XPS, Thermoscience Co., Ltd., Waltham, USA) was used to explore the valence state and the form of metal compounds. The composition and valence state of the compounds can be determined by determining the peak position of the scanned curve and measuring the peak spacing. The prepared catalyst materials were crushed and fully mixed in KBr for FT-IR analysis. The mixture was pressed on the work-table for scanning electron microscope observations. The range of infrared spectrum was 4000-400 cm^{-1} , and the scanning resolution was higher than 0.09 cm^{-1} .

3 Results And Discussion

3.1 SDBD and DDBD treatment of benzene series

3.1.1 Discharge parameters and air tube analysis

Discharge parameters are an essential aspect for the performance of DBD reactor. Through different output voltages, different discharge powers of SDBD and DDBD were obtained (Fig. S1). The discharge power of DDBD was higher than that of SDBD under different output voltages. With the increase in voltage, the difference in the discharge power increased gradually, reaching the value of 15.5 W. Fig. 2 showed the relationship between SED, airflow and output voltage. For a certain voltage, with the increase of flow rate, the reactor's SED decreased gradually, whereas SDBD attenuated faster than the DDBD. For a constant airflow, the SED increased gradually with the increase of output voltage. Compared with the DDBD, the SED of SDBD increased slightly. It can be seen that, in the DBD, the SED was positively correlated with the output voltage and negatively correlated with the airflow. The preservation capability of SDBD for SED was weaker than that of DDBD.

3.1.2 Effect of initial concentration on the degradation rate and by-products

The degradation efficiencies of SDBD and DDBD for benzene and toluene mixture decreased gradually with the increase of initial concentration, and the degradation rate decreased from the highest value of 78% to the lowest value of 3% (Fig. 3). When the energy density was kept constant, the high-energy electrons and active particles were limited with the increase of pollutant concentration. The removal rate decreased with the increase of initial concentration. The removal rate of VOCs in DDBD was higher than that of SDBD because the SED of DDBD was higher than that of SDBD and released more electricity. The degradation rate of toluene was significantly higher than that of benzene (about 11 - 21% higher), which was due to the fact that toluene has one more methyl entity than benzene that is easier to fall off (Wu et al., 2013; Liu et al., 2017; Najafpoor et al., 2018; Dang et al., 2016). The EEs of the two reactors for the VOCs' mixture were different from each other. The EE of DDBD was slightly higher than that of SDBD by 0.1 - 0.25 g/kWh (Fig. 3), indicating that the EEs of the two reactors for benzene and toluene treatment were not significantly different because the SED of the two reactors was constant. The SED and degradation efficiency of DDBD for toluene, and benzene were higher than those of SDBD. From the perspective of the reactor structure, the discharge breakdown of a single medium was relatively easy. The two layers of the medium increased the thickness of barrier, which led to increased energy consumption and reduced EE. With the increase in the initial concentrations of benzene and toluene, the overall EE first increased, became flat, and then, decreased. In the case of constant SED, the electric energy generated by the device was constant, and the active substances in the device were constant. With the increase in the concentration of benzene series, the increased by-products consumed more electricity, which degraded the pollutants. However, when the increase in the initial concentration reached to a certain extent, the need for electric energy was limited, which interfered with the by-products. Therefore, the degradation efficiency and energy utilization rate decreased for the process.

In the air tube (Fig. S2) with the output voltage of 12 kV and flow rate of 275 L/h, O₃ concentration produced by SDBD was about 3787.43 ppm, and that produced by DDBD was about 2144.47 ppm. For the constant SED, the transformation rate of O₃ increased with the build-up of output voltage (Fig. 4a), indicating that part of O₃ generated by the plasma device was involved in the degradation of VOCs, while some part of O₃ got transformed and degraded (Mao et al., 2017; Chen et al., 2018). The higher the benzene series concentration, the more O₃ consumption. When the concentration increased to about 100 ppm, the consumption rate of O₃ was slower than in the previous stage. The concentration of NO₂ in SDBD was 196.54 ppm, whereas that in DDBD was 73.21 ppm. Fig. 4b showed that, when the initial concentration was 20-80 ppm, NO₂ in SDBD was slightly higher than that in DDBD. After 80 ppm, the transformation rate of NO₂ in DDBD was higher than that in SDBD, which may be due to the presence of minor ·O and other substances in SDBD compared to DDBD. With the increase of concentration, limited ·O preferentially participated in the degradation of VOCs and intermediates, which reduced the transformation of NO₂ in SDBD. The fluctuation in the rate of transformation of NO₂ in SDBD was unstable, which may have been caused by the instability of SDBD.

The concentration of NO was 13.25 ppm in SDBD and 0.981 ppm in DDBD. As the initial concentration of VOCs increased, the transformation rate of NO in SDBD increased significantly (Fig. 4c), which was due to the reason that there were more substances such as ·O in SDBD than in DDBD that contributed to the transformation of NO into NO₂. Fig. 4d shows the relationship between the CO₂ selectivity and the degradation of benzene and toluene in the two reactors. The mineralization of SDBD was slightly lower than that of DDBD during the degradation of benzene. The mineralization of the two reactors gradually decreased with the increase of initial concentration. The reason why the mineralization of SDBD was lower than that of DDBD was that the discharge of DDBD was stable and more active substances were produced in stable states. Furthermore, more active substances were involved in the process of ring-opening of benzene and toluene, which effectively degraded the VOCs and converted them into CO₂. The efficiency was higher, so the CO₂ selectivity of DDBD was higher than that of SDBD. For the phenomenon that the degree of mineralization decreased with the increase in the concentration of VOCs. This could be due to the reason that the SED was constant, and the total amount of active substances were also constant. When the concentration of VOCs increased, the limited active substances were not sufficient to transform VOCs into CO₂, resulting in an increase in the intermediate products, which led to a decrease in the selectivity of CO₂. The second reason is that, with the increase in the concentration of VOCs, the intermediate products increased, which increased the consumption of electricity and led to a decrease in the degree of mineralization. In addition, the selectivity of CO₂ in SDBD was relatively unstable, which was caused by the unstable discharge of electric energy and the unstable amount of intermediate products.

3.1.3 Effect of output voltage on the degradation rate and by-products

As the output voltage increased, the degradation rate of VOCs became larger (Fig. S3), which was due to the increase in the electric field's intensity and more active substances, thus improving the efficiency of the degradation of VOCs. For the same output voltage, the degradation efficiency of VOCs of SDBD was lower than that of DDBD because the DDBD was more stable and produced more effective active substances, thereby improving the degradation efficiency of VOCs. The output voltage was positively correlated with the EE (Fig. S3). As the SED increased, the electric field intensity increased, and the active substances increased the species involved in the degradation of VOCs, which in turn increased the energy efficiency. Beyond the voltage of 13 kV, the energy efficiency could not be increased. Although the active substances produced by the reactor increased, the concentration of the degraded target pollutants became limited, and therefore, the EE became limited.

When the concentration of VOCs, flowrate and output voltage had values of 110 ppm, 275 L/h, and 10-13 kV, the transformation rate of O_3 increased with the increase of voltage (Fig. S4a). Due to the increase of SED, although the generated O_3 increased, the active substances increased as well. Most of the O_3 transformed into active substances and participated in the degradation reactions of VOCs. When the output voltage lied within the range of 13–16 kV, with the increase of voltage, the O_3 transformation rate decreased. Moreover, the O_3 concentration generated at this stage increased sharply, and the concentration of VOCs was limited. The excess O_3 cannot participate in the transformation, so the transformation rate decreased. Within the output voltage range, the difference of O_3 transformation between the two reactors was not obvious. The transformation rate of NO_2 in SDBD was higher than that in DDBD after the output voltage of 10 kV (Fig. S4b). When the concentration and flow rate of VOCs were constant, the build-up of voltage led to the increase of active substances and the consumption of more $\cdot O$, which reduced the formation of NO_2 and increased the number of intermediate products. The generated NO was involved in the degradation of intermediate products, which also reduced NO_2 . In addition, the increase of O_3 concentration also promoted the transformation of NO_2 . The transformation rates of NO and NO_2 in SDBD were also higher than those in DDBD (Fig. S4c).

The degree of mineralization of SDBD in benzene degradation was significantly lower than that of DDBD (Fig. S4d). DDBD generated electrical energy more stably than SDBD, which in turn generated more active substances consistently. More active substances were involved in the ring-opening process of benzene and toluene (Han et al., 2020), which improved the degradation efficiency of VOCs into CO_2 . Therefore, DDBD had higher CO_2 selectivity than the SDBD. Similarly, the mineralization of DDBD was higher than that of SDBD. Beyond the output voltage of 12-13 kV, the selectivity of CO_2 tended to stabilize. When the intermediate product increased to the maximum, it gradually degraded into CO_2 and reached a certain degree of stability. Even if the active substance increased, the mineralization did not change, and the selectivity of CO_2 tended to stabilize.

3.1.4 Effect of airflow on the degradation rate and by-products

The degradation efficiency of VOCs by SDBD and DDBD decreased with the increase of flow rate (Fig. S5). Due to the decrease of residence time, the contact time between the VOCs and active substances decreased. The energy efficiency of SDBD was higher than that of DDBD (Fig. S5). With the increase in the flow rate, the energy efficiency increased. When the concentration of VOCs and the output voltage were constant, SED decreased, and the degradation rate of VOCs exhibited little change, which led to an increase in energy efficiency. However, due to the limitation of residence time, the energy efficiency increased slightly.

With the change in the gas flow rate, the transformation rate of O_3 fluctuated significantly (Fig. S6a) because the formation and transformation of O_3 were greatly affected by the residence time. Another reason was that the flow had a significant impact on SED. The overall performance of DDBD for O_3 transformation was better than SDBD because DDBD discharge was more stable. Furthermore, its SED was less affected by flow than that of SDBD, and therefore, it would produce more active substances to promote the transformation of O_3 . The transformation rates of NO_2 and NO both decreased with the increase of airflow (Fig. S6b). There was little difference between the SDBD and DDBD for the transformation of NO_2 . The transformation of NO in SDBD was higher than that in DDBD (Fig. S6c). This could be due to two reasons. The first was the shorter residence time and the shorter contact reaction time for NO_2 and active substances. The second was that the SED decreased with the increase in the flow rate, and the amount of active substance produced decreased.

With the increase in the flow rate, the mineralization of SDBD and DDBD gradually decreased, which was also consistent for the degradation of toluene (Fig. S6d). This could be due to the reason that both the SED and the number of active substances decreased. The limited active substances were not sufficient to degrade benzene and toluene to CO_2 , resulting in an increase in the intermediate products and a decrease in the selectivity of CO_2 . The second reason was that the residence time decreased, due to which, the contact time between the intermediate products and the active substances decreased, thus decreasing the degree of mineralization. SDBD was slightly less mineralized than DDBD during the degradation of benzene.

3.2 Preparation of rGO-based catalyst

3.2.1 Preparation of GO

The FG morphology was stacked. The layers were closely connected, while the edges were clearly defined and compact (Fig. 5a). Both the GO1 and GO2, prepared using different methods (Fig. 5b,c), were significantly different from flake graphite in morphology after the IHM and ultrasonic exfoliation. For GO1, although the layer spacing increased, the morphology and appearance were not ideal. The degree of oxidation stripping was also not high. On the other hand, by adding $KMnO_4$ in multiple batches, GO2 was intercalated by orderly oxidation. GO2 was complete and orderly than GO1.

BET surface area (S_{BET}), total pore volume (V_{total}), and average pore diameter (d_{pore}) of the flake graphite were low, and the two kinds had significant differences compared with the FG (Table S1). The physical performance was significantly improved, and the preparation of GO from the flake graphite was relatively complete. Furthermore, S_{BET} of GO2 increased by about 11% compared with GO1, however V_{total} and d_{pore} did not increase significantly.

XRD characterization (Fig. 6a) showed that the FG had a characteristic graphite peak at 26.5° , whereas both the GO1 and GO2 had a characteristic peak of GO at 10.6° , and 42.5° . According to Bragg's law, the layer spacing of GO2 was nearly three times larger than that of FG, indicating that introduction of KMnO_4 in batch mode can effectively increase the layer spacing of GO.

Figure 6b showed no peak of FG, indicating that there was no functional group. A series of characteristic peaks appeared in GO2, indicating that the polar groups increased sharply, and O-H appeared at 3375 cm^{-1} . The absorption peak at 1621 cm^{-1} belonged to the unoxidized vibration peak of C=C, whereas the absorption peak at 1261 cm^{-1} was ascribed to the C-H stretching vibration (Kizil et al., 2002; Almasian et al., 2010). The absorption peak at 1135 cm^{-1} was ascribed to C-O-C. These polar functional groups all indicated that GO introduced more hydrophilic groups, which is also the reason for GO's hydrophilic solid properties.

3.2.2 Preparation of catalyst using ion-assisted hydrothermal method

In the absence of [BMIM]PF₆, the nanocrystals showed irregular morphology and local dispersion, whereas most of them had severe agglomeration (Fig. 7a). The manganese catalyst was effectively dispersed on the rGO after the addition of [BMIM]PF₆. The addition of [BMIM]PF₆ could effectively improve the degree of dispersion and reduce the degree of agglomeration (Fig. 7b). The excessive addition of [BMIM]PF₆ made the nanocrystals exhibit irregular morphology, and the agglomeration phenomenon occurred locally (Fig. 7c).

When [BMIM]PF₆ was not added, the formation of crystals was incomplete, and the layer edge was crimped, which is not conducive to the presence of nucleation center of the catalyst (Fig. 7d). When the dosage of [BMIM]PF₆ was 0.25 mL, the morphology and structural characteristics of the prepared FeO_x/rGO catalyst were apparent. The crystal dispersion was a little high (Fig. 7e). When the dosage of [BMIM]PF₆ was 0.5 mL, the crystal dispersion was not too high (Fig. 7f). The TiO_x/rGO catalyst prepared with the addition of 0.25 mL of [BMIM]PF₆ had good structural morphology (Fig. 7g). The crystal formation of 0 mL (Fig. 7h) and 0.5 mL (Fig. 7i) was not complete, and the lamellar edges were crimped, which was not conducive to nucleation.

Within the 0-0.25 mL range, the S_{BET} and V_{total} of the three catalysts increased, whereas d_{pore} decreased. Within the range of the added amount of 0.25-0.5 mL, excessive addition led to poor dispersion performance of the catalyst, agglomeration and other phenomena, which all resulted in smaller specific

surface areas (Table S2). When the dosage of [BMIM]PF₆ was 0.25-0.5 mL, S_{BET} , V_{total} , and d_{pore} of the three catalysts showed little change.

In the absence of [BMIM]PF₆, the characteristic peaks of MnO_x/rGO with different intensities appeared. When 0.25 mL [BMIM]PF₆ was added, some characteristic peaks of Mn₃O₄ appeared (Fig. 8a). When there was no [BMIM]PF₆, there were two characteristic peaks of FeO_x/rGO at 27.3° and 42.5°, both of which belonged to Fe₃O₄ (JDPDF 26-1136). When 0.5 mL of [BMIM]PF₆ was added, the characteristic peak at 27.3° was weaker than that when there was no [BMIM]PF₆, while the characteristic peak at 42.5° became narrower and sharper. Compared with the characteristic diffraction peak when 0.5 mL of [BMIM]PF₆ was added, the characteristic peak at 0.25 mL was sharper, narrower and higher in intensity, indicating that better crystals were formed due to relatively intact lattices and a higher degree of crystallization under the condition of 0.25 mL of ion-assisted solution (Fig. 8b). All diffraction peaks of TiO_x/rGO catalyst belonged to TiO₂ (JDPDF 21-1272). With the increase in the dosage of [BMIM]PF₆, the diffraction peak of C=O gradually weakened (Fig. 8c).

Figure S7a shows the FT-IR characteristics of three catalysts prepared with different additives. The MnO_x/rGO prepared without [BMIM]PF₆ had an O-H vibration stretching peak at 3487 cm⁻¹, while the addition of 0.25 mL [BMIM]PF₆ significantly weakened its peak intensity and introduced some new groups (O-H group, H₂O group, and C-O-H group). Moreover, the addition of 0.5 mL [BMIM]PF₆ had no prominent characteristic peak compared with the first two, which may be due to the addition of too much ionic liquid that resulted in incomplete hydrothermal reduction reaction and crystallization of [BMIM]PF₆ without introducing more new groups. For FeO_x/rGO, when [BMIM]PF₆ dosage was 0-0.25 mL, there was an O-H stretching vibration peak at 3487 cm⁻¹, whereas the peak intensity decreased for the added amount of 0.5 mL (Fig. S7b). The more substantial characteristic peak (O-H group) at 3487 cm⁻¹ was of the 0.5 mL [BMIM]PF₆ dosage spectrum. In contrast, the characteristic peak intensity of [BMIM]PF₆ for 0 mL and 0.25 mL was slightly weaker (Fig. S7c). For the three dosage conditions of the ionic liquid, the preparation results of the catalyst were ideal when the [BMIM]PF₆ dosage was 0.25 mL. The crystal had enhanced physical properties, many active centers for the nucleation of catalyst, and its internal structure and functional groups were excellent.

3.3 DDBD combined with the three catalysts

3.3.1 Degradation of benzene series using MnO_x/rGO, FeO_x/rGO, TiO_x/rGO combined with DDBD system

The degradation rate of MnO_x/rGO+DDBD was the highest among the four combinations of benzene and toluene degradation (Fig. 9a), with the value for benzene reaching to around 82% and that for toluene 86%. Compared to the DDBD device without a catalyst system, the degradation rate increased by 20-43%. The degradation efficiency of FeO_x/rGO+DDBD was second only to MnO_x/rGO+DDBD, which was determined by the properties of Mn and Fe catalysts (Qin et al., 2021). In another words, VOCs and active

substances induced a redox reaction on the surface of the catalyst, and its degradation capability was closely related to the redox capability of the catalyst itself. Mn has a stronger catalytic capacity and higher redox capacity (Durán et al., 2009). The degradation efficiency of $\text{TiO}_x/\text{rGO}+\text{DDBD}$ was lower than the first two, among which TiO_x/rGO mainly relied on the ultraviolet (UV) light generated by plasma to trigger the catalytic effect (Zhao et al., 2015; Souza et al., 2006; Brückner et al., 2021). However, this system consisted of a series device. The UV light generated by DBD was relatively weak on the catalyst at the tail end, due to which, its catalytic effect was not very ideal. The EE of $\text{MnO}_x/\text{rGO}+\text{DDBD}$ was the highest (Fig. 9b), which was 31-54% higher than that of DDBD without a catalytic system. The EE was related to the SED and degradation efficiency. The degradation efficiency of the $\text{MnO}_x/\text{rGO}+\text{DDBD}$ system was the highest, and its energy efficiency was also the highest.

The O_3 transformation rate of $\text{FeO}_x/\text{rGO}+\text{DDBD}$ was the highest (Fig. 9c), reaching the value of about 80%. Compared with the DDBD without a catalyst system, the O_3 transformation rate of $\text{FeO}_x/\text{rGO}+\text{DDBD}$ increased by about 43.5% because the introduced FeO_x/rGO transformed the excess O_3 into active substances, such as superoxide free radicals. The NO transformation of $\text{MnO}_x/\text{rGO}+\text{DDBD}$ was about 71%, and the NO_2 transformation was about 73%, which was about 47% higher than a single DDBD processing unit. The $\text{MnO}_x/\text{rGO}+\text{DDBD}$ system had the highest degree of mineralization (Fig. 9d). The reaction of active substances with manganese-based catalysts resulted in more VOCs being effectively degraded and more intermediate products transformed into CO_2 .

3.3.2 XPS characterization of the three catalysts

The most obvious atomic content was that of C, followed by O (Table S3). Catalysts were combined with graphene to produce -COOH. The surface of the catalyst adsorption caused $-\text{OH}/\text{CO}_3^{2-}$. Moreover, O^{2-} was combined with the three transition metal lattice oxygen. The oxygen content of the three transition metal catalysts included adsorbed water (-COOH), adsorbed oxygen on the surface of the catalyst ($-\text{OH}/\text{CO}_3^{2-}$), and lattice oxygen (O^{2-}) (Huang et al., 2012; He et al., 2019; Zeng et al., 2019; Kara et al., 2014). Overall, the proportion of each catalyst was not much different from the theoretical value (Fig. 10a). MnO_x/rGO catalyst contained the highest content of lattice oxygen, whereas TiO_x/rGO catalyst had the most surface adsorbed oxygen. Moreover, FeO_x/rGO lied in between the two (Fig. 10b). Generally speaking, lattice oxygen and surface adsorbed oxygen often determine the excellent catalytic performance. Therefore, all the three transition metals had a high catalytic capability.

In the high-resolution spectra, manganese mainly existed in the form of Mn_{2p1} and Mn_{2p3} , whereas iron mainly existed in the form of Fe_{2p1} . Furthermore, titanium mainly existed in the form of Ti_{2p3} . The high-resolution O_{1s} spectrum was assigned to -COOH at 532.1 eV, to $-\text{OH}/\text{CO}_3^{2-}$ at 531.4 eV, and to O^{2-} at 530.9 eV. For the high-resolution spectral image of Mn_{2p} (Fig. 10c), a prominent characteristic peak near 653.8 eV belonged to Mn_{2p1} . At the binding energy of 642.1 eV, its characteristic peak belonged to Mn_{2p3} . According to the comparison of XPS binding energies and spacing, MnO_x/rGO catalyst mainly existed as Mn_3O_4 . For Fe_{2p} high-resolution spectrograph (Fig. 10d), the characteristic peak was not apparent at

724.7 eV, which should belong to Fe_{2p1} . The characteristic peak of Fe_{2p3} (710.3 eV) was more potent than that of Fe_{2p3} . According to the XPS Binding Energy (B.E.) results and the binding energy spacing, FeO_x/rGO catalyst mainly existed in the form of Fe_3O_4 . In the Ti_{2p} spectrum (Fig. 10e), the characteristic peak at the binding energy of 464.9 eV belonged to Ti_{2p1} , whereas the characteristic peak at the binding energy of 1458.2 eV belonged to Ti_{2p3} . According to the XPS B.E. results and spacing, the TiO_x/rGO catalyst mainly existed as TiO_2 .

4 Conclusion

The degradation rate of DDBD to benzene series was higher than that of SDBD, and EE of DDBD and SDBD were close. The NO_2 transformation rate of DDBD was higher than that of SDBD. Although the NO transformation rate of SDBD was higher than that of DDBD, the NO concentration was very low and can be ignored. There was little difference between SDBD and DDBD in the O_3 transformation performance, and the mineralization of DDBD was higher than SDBD. The best preparation method of GO was when KMnO_4 solution was added four times, and the interval was less than 10 min. The morphology and internal structure of MnO_x/rGO and FeO_x/rGO were the best in dosages of 0.25 mL [BMIM]PF₆. For TiO_x/rGO catalyst, the dosages of 0.25 mL and 0.5 mL [BMIM]PF₆ had no significant difference.

The results showed that rGO/MnO_x +DDBD had the best performance in the degradation of benzene series, NO_2 transformation rate, NO transformation rate and mineralization. The rGO/FeO_x has the highest transformation performance for O_3 . Combined with the experimental performance and the XPS characterization results, Mn_3O_4 exhibited high performance in the degradation of benzene series, NO transformation, CO_2 selectivity and EE. Fe_3O_4 showed high performance in the degradation of benzene series and O_3 transformation.

Declarations

Ethical Approval

There are no ethical issues in this article.

Consent to Participate

All the authors agree to participate in this paper.

Consent to Publish

All the authors agree to the publication of this paper.

Authors Contributions

Mr. Zongyang Liu did research experiments and analyzed the data; Mr. Yifan Wang, Mr. Gengmeng Zhang, and Miss Jie Yang did the other experiments; Mr. Zongyang Liu along with Prof. Shengyu Liu, led the writing of the manuscript.

Fundings

Financial supports for this project were provided by National Natural Science Foundation of China (No.21676032), Key Research and Development Project Foundation of Science and Technology Department of Sichuan Province (No. 2020YFS0342), Education Department of Sichuan Province (No.14TD0020), Chengdu Science and Technology Bureau (No. 2016-GH02-00032-HZ), which are greatly acknowledged.

Competing Interests

The authors declare no competing interests.

Availability of data and materials

All data generated or analyzed during this study are included in this published article.

References

1. Almasian MR, Na N et al (2010) Development of a plasma-assisted cataluminescence system for benzene, toluene, ethylbenzene, and xylenes analysis. *Anal Chem* 82(9):3457. <https://doi.org/10.1021/ac1006975>
2. Alqahtani MS, Wang XX et al (2020) Plasma-assisted catalytic reduction of so₂ to elemental sulfur: influence of nonthermal plasma and temperature on iron sulfide catalyst. *J Catal* 391:260–272. <https://doi.org/10.1016/j.jcat.2020.08.013>
3. An T, Huang Y et al (2014) Pollution profiles and health risk assessment of vocs emitted during e-waste dismantling processes associated with different dismantling methods. *Environ Int* 73:186–194. <https://doi.org/10.1016/j.envint.2014.07.019>
4. Brückner Lea, Beyer-Westendorf J et al (2021) Development and validation of an analytical method for the determination of direct oral anticoagulants (doac) and the direct thrombin-inhibitor argatroban by hplc-ms/ms. *J Thromb Thrombolysis* 15(3):103663. <https://doi.org/10.1016/j.arabjc.2021.103663>
5. Chen B, Gao X et al (2018) Regulation characteristics of oxide generation and formaldehyde removal by using volume dbd reactor. *Plasma Sci Technol* 20:024009. <https://doi.org/10.1088/2058-6272/aa9b7a>
6. Dang X, Qin C et al (2016) Adsorbed benzene/toluene oxidation using plasma driven catalysis with gas circulation: elimination of the byproducts. *J Ind Eng Chem* 366–371. <https://doi.org/10.1016/j.jiec.2016.03.051>

7. Durán FG, Barbero BP et al (2009) Manganese and iron oxides as combustion catalysts of volatile organic compounds. *Applied Catalysis B Environmental* 92(1–2):194–201. <https://doi.org/10.1016/j.apcatb.2009.07.010>
8. Ehn M, Thornton J et al (2014) A large source of low-volatility secondary organic aerosol. *Nature* 506:476–479. <https://doi.org/10.1038/nature13032>
9. Fang BY, Guo FY et al (2018) *Phyllostachys edulis* forest reduces atmospheric pm2.5 and pahs on hazy days at suburban area. *entific Reports* 8(1):12591. <https://doi.org/10.1038/s41598-018-30298-9>
10. Hao Z, Ji S (2012) Optical and electric diagnostics of DBD plasma jet in atmospheric pressure Argon. *International Conference on Condition Monitoring & Diagnosis. IEEE*, 1187–1190. <https://doi.org/10.1109/CMD.2012.6416373>
11. Han F, Li M et al (2020) Product analysis and mechanism of toluene degradation by low temperature plasma with single dielectric barrier discharge. *Journal of Saudi Chemical Society* 24(9):673–682. <https://doi.org/10.1016/j.jscs.2020.07.004>
12. He C, Cheng J et al (2019) Recent Advances in the Catalytic Oxidation of Volatile Organic Compounds: A Review Based on Pollutant Sorts and Sources. *Platin Met Rev* 119(7):109–113. <https://doi.org/10.1021/acs.chemrev.8b00408>
13. Herrera FA, Brown et al (2019) The impact of transition metal catalysts on macroscopic dielectric barrier discharge (dbd) characteristics in an ammonia synthesis plasma catalysis reactor. *Journal of Physics D Applied Physics* 224002–224002. <https://doi.org/10.1088/1361-6463/ab0c58>
14. Huang K, Zhuang G et al (2012) Typical types and formation mechanisms of haze in an eastern asia megacity, shanghai. *Atmos Chem Phys* 12(1):105–124. <https://doi.org/10.5194/acp-12-105-2012>
15. Huang HF, Chu X et al (2011) Dynamic adsorption performances and breakthrough curve model of some aromatic vocs on mcm-41 and sba-15. *Journal of Chemical Engineering of Chinese Universities* 25(2):219–224. <https://doi.org/10.3354/cr00999>
16. Ji HB, Santos CA et al (2021) Energy efficient treatment of indoor volatile organic compounds using a serial dielectric barrier discharge reactor. *Process Saf Environ Prot* 153:29–36. <https://doi.org/10.1016/j.psep.2021.07.009>
17. Kara M, Dumanoglu Y et al (2014) Seasonal and spatial variations of atmospheric traceelemental deposition in the aliaga industrial region, turkey. *Atmos Res* 43(3):109–113. <https://doi.org/10.1016/j.atmosres.2014.06.009>
18. Kizil R, Irudayaraj J et al (2002) Characterization of irradiated starches by using ft-raman and ftir spectroscopy. *Journal of Agricultural & Food Chemistry* 50(14):3912–3918. <https://doi.org/10.1021/jf011652p>
19. Li H, Wang Y, Liu F et al (2018) Volatile organic compounds in stormwater from a community of beijing, china. *Environ Pollut* 239:554–561. <https://doi.org/10.1016/j.envpol.2018.04.065>
20. Lian Y, Long W et al (2017) Adsorption of vocs on reduced graphene oxide. *J Environ Sci* 67(5):171–178. <https://doi.org/10.1016/j.jes.2017.08.022>

21. Liang P, Jiang W et al (2015) Experimental studies of removing typical VOCs by dielectric barrier discharge reactor of different sizes. *Process Safety & Environmental Protection* 94:380–384. <https://doi.org/10.1016/j.psep.2014.09.003>
22. Liu L, Qiang W et al (2017) Plasma-assisted catalytic reforming of toluene to hydrogen rich syngas. *Catal Sci Technol* 18:4216–4231. <https://doi.org/10.1039/c7cy00970d>
23. Luo H, Li G et al (2020) Spatial and temporal distribution characteristics and ozone formation potentials of volatile organic compounds from three typical functional areas in China. *Environ Res* 183:109141. <https://doi.org/10.1016/j.envres.2020.109141>
24. Mao L, Chen Z, Fu MF et al (2017) X., 2018. Volatile organic compounds (VOCs) removal in non-thermal plasma double dielectric barrier discharge reactor. *Journal of Hazardous Materials*,347, 317-324. <https://doi.org/10.1016/j.jhazmat.2018.01.021>
25. Mishra RK, Upadhyay SB et al (2013) Volatile organic compounds (VOCs) response characteristics of the hydrothermally synthesized SnO₂ nanocapsules. *Sens Lett* 11(9):1611–1616. <https://doi.org/10.1166/sl.2013.3020>
26. Najafpoor AA, Jonidi JA et al (2018) Optimization of non-thermal plasma efficiency in the simultaneous elimination of benzene, toluene, ethyl-benzene, and xylene from polluted airstreams using response surface methodology. *Environmental Science & Pollution Research* 154(1):506–512. <https://doi.org/10.1007/s11356-017-0373-8>
27. Park JH, Goldstein AH et al (2013) Active atmosphere-ecosystem exchange of the vast majority of detected volatile organic compounds. *Science* 341(6146):643–647. <https://doi.org/10.1126/science.1235053>
28. Qin C, Guo M et al (2021) Simultaneous oxidation of toluene and ethyl acetate by dielectric barrier discharge combined with Fe, Mn and Mo catalysts. *Sci Total Environ* 782:146931. <https://doi.org/10.1016/j.scitotenv.2021.146931>
29. Ran J, Qiu H et al (2018) Are ambient volatile organic compounds environmental stressors for heart failure? *Environ Pollut* 242:1810–1816. <https://doi.org/10.1016/j.envpol.2018.07.086>
30. Souza RMD, Meliande A et al (2006) Determination of Mo, Zn, Cd, Ti, Ni, V, Fe, Mn, Cr and Co in crude oil using inductively coupled plasma optical emission spectrometry and sample introduction as detergentless microemulsions. *Microchem J* 82(2):137–141. <https://doi.org/10.1016/j.microc.2006.01.005>
31. Tseng TK, Lin YS et al (2010) A review of photocatalysts prepared by sol-gel method for VOCs removal. *Int J Mol Sci* 11(6):2336–2361. <https://doi.org/10.3390/ijms11062336>
32. Wu J, Huang Y et al (2013) Decomposition of toluene in a plasma catalysis system with NiO, MnO₂, CeO₂, Fe₂O₃, and CuO catalysts. *Plasma Chem Plasma Process* 33(6):1073–1082. <https://doi.org/10.1007/s11090-013-9485-1>
33. Yao X, Zhang J et al (2018) Plasma-catalytic removal of toluene over the supported manganese oxides in DBD reactor: effect of the structure of zeolites support. *Chemosphere* 208:922–930. <https://doi.org/10.1016/j.chemosphere.2018.06.064>

34. Yao X, Zhang J et al (2019) Niobium doping enhanced catalytic performance of mn/mcm-41 for toluene degradation in the ntp-catalysis system. *Chemosphere*, 230, 479-487.
<https://doi.org/10.1016/j.chemosphere.2019.05.075>
35. Yu H, Hu W et al (2019) Decomposition efficiency and aerosol by-products of toluene, ethyl acetate and acetone using dielectric barrier discharge technique. *Chemosphere* 237:124439.
<https://doi.org/10.1016/j.chemosphere.2019.124439>
36. Yukimura K, Kawamura K et al (2005) Correlation of energy efficiency of no removal by intermittent dbd radical injection method. *IEEE Trans Plasma Sci* 33(2):763–770.
<https://doi.org/10.1109/TPS.2005.844610>
37. Zeng X, Li B et al (2019) Investigation of promotion effect of cu doped mno2 catalystson ketone-type vocs degradation in a one-stage plasma-catalysis system. *Chem Eng J* 384:123362.
<https://doi.org/10.1016/j.cej.2019.123362>
38. Zhang HB, Li K et al (2014) Enhancement of styrene removal using a novel double-tube dielectric barrier discharge (DDBD) reactor. *Chem Eng J* 256:107–118.
<https://doi.org/10.1016/j.cej.2014.06.105>
39. Zhang X, Xue Z et al (2017) Ambient volatile organic compounds pollution in china. *J Environ Sci*.
<https://doi.org/10.1016/j.jes.2016.05.036>
40. Zhao LC, Guo XP et al (2015) Simultaneous determination of major elements si,al,ca,mg,fe,ti,mn and p in graphite by inductively coupled plasma-optical emission spectrometrywith sodium carbonate fusion. *Rock and Mineral analysis* 3308–313. <https://doi.org/10.15898/j.cnki.11-2131/td.2015.03.008>
41. Zhu X, Liu Y (2014) Characterization and risk assessment of exposure to volatile organiccompounds in apartment buildings in harbin, china. *Bull Environ Contam Toxicol* 92(1):96.
<https://doi.org/10.1007/s00128-013-1129-x>

Tables

Table 1 Specific surface area, pore volume and pore diameter of FG, G01 and G02.

Sample	S_{BET} /m ² /g	V_{total} /cm ³ /g	d_{pore} /nm
FG	4.32	0.003	0.43
G01	254	0.7121	6.38
G02	285	0.899	7.54

S_{BET} : BET surface area, V_{total} : total pore volume, d_{pore} : average pore diameter

Table 2 Surface Area, Pore Volume and Pore Size of rGO/MnO_x, rGO/FeO_x and rGO/TiO_x Prepared with Different Doses of [BMIM]PF₆.

Sample	S_{BET} [m ² /g]	V_{total} [cm ³ /g]	d_{pore} [nm]
MnO _x /rGO _(0ml)	206	0.386	3.62
MnO _x /rGO _(0.25ml)	221	0.511	3.28
MnO _x /rGO _(0.5ml)	196	0.284	2.71
FeO _x /rGO _(0ml)	207	0.341	3.18
FeO _x /rGO _(0.25ml)	219	0.411	3.07
FeO _x /rGO _(0.5ml)	174	0.328	4.69
TiO _x /rGO _(0ml)	204	0.382	4.81
TiO _x /rGO _(0.25ml)	221	0.511	3.28
TiO _x /rGO _(0.5ml)	219	0.504	3.16

S_{BET} : BET surface area, V_{total} : total pore volume, d_{pore} : average pore diameter

Figures

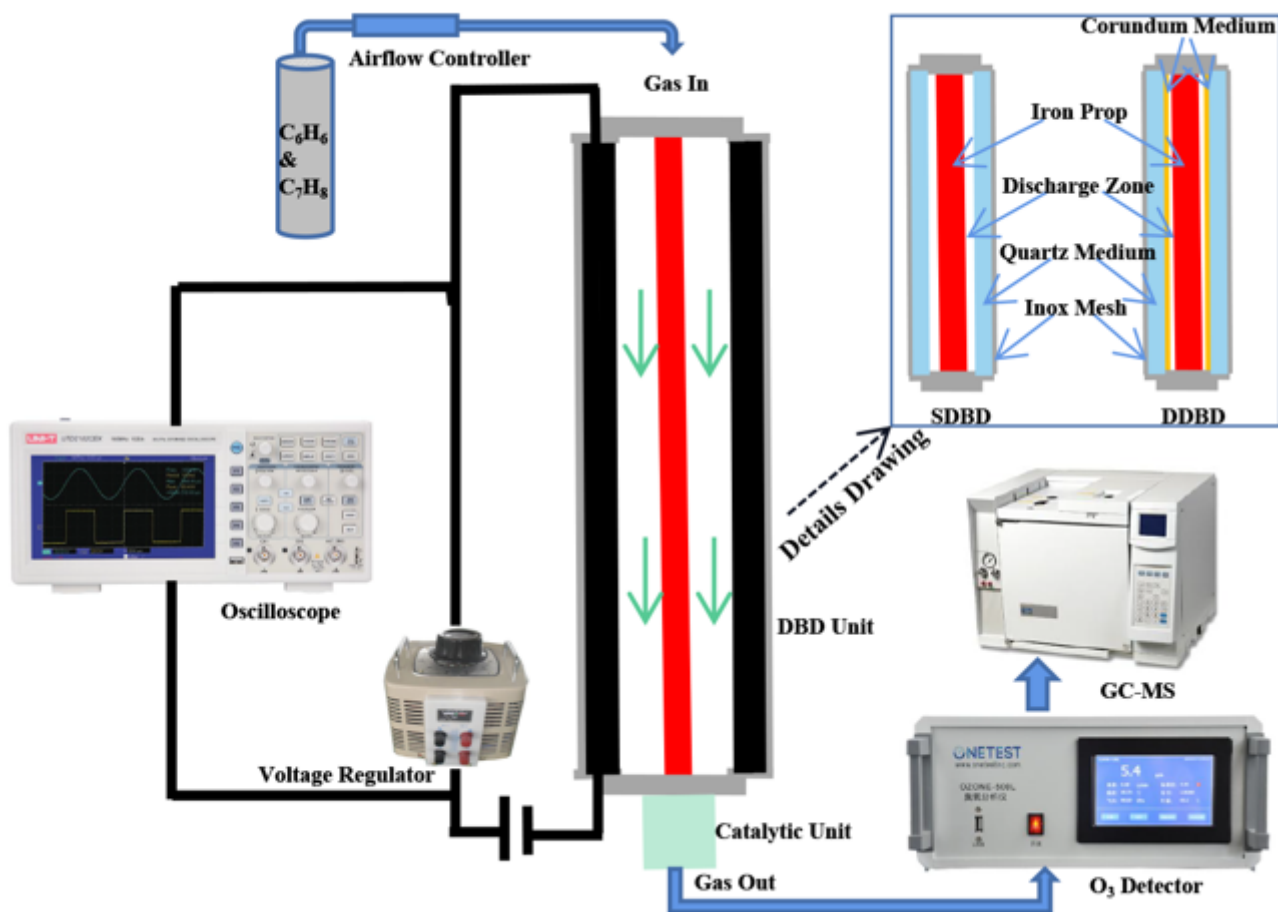


Figure 1

Experimental flow and reactors structure

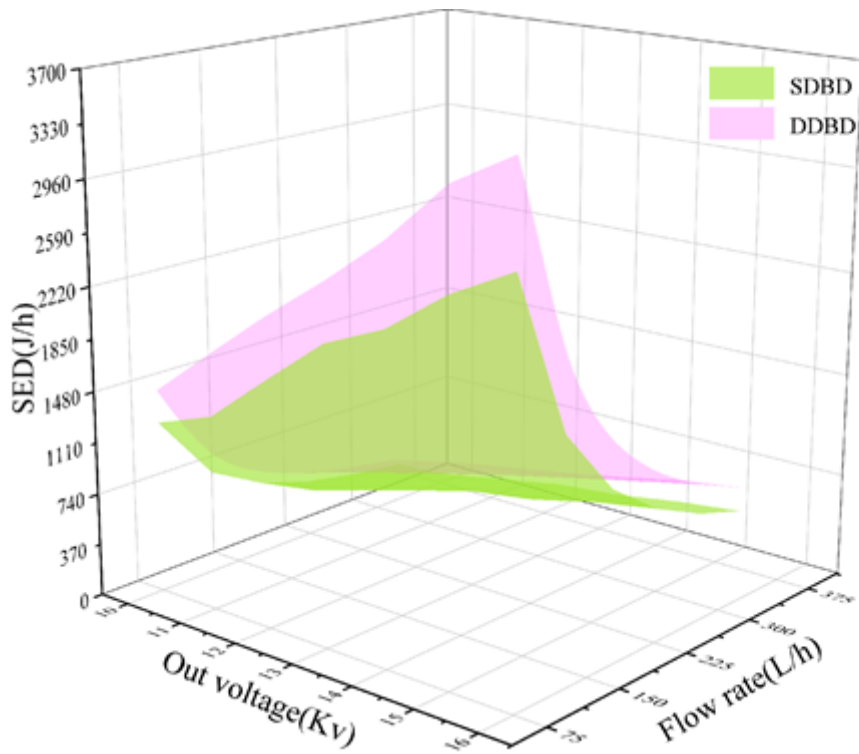


Figure 2

Relationship between SED and output voltage, flow variation of SDBD and DDBD

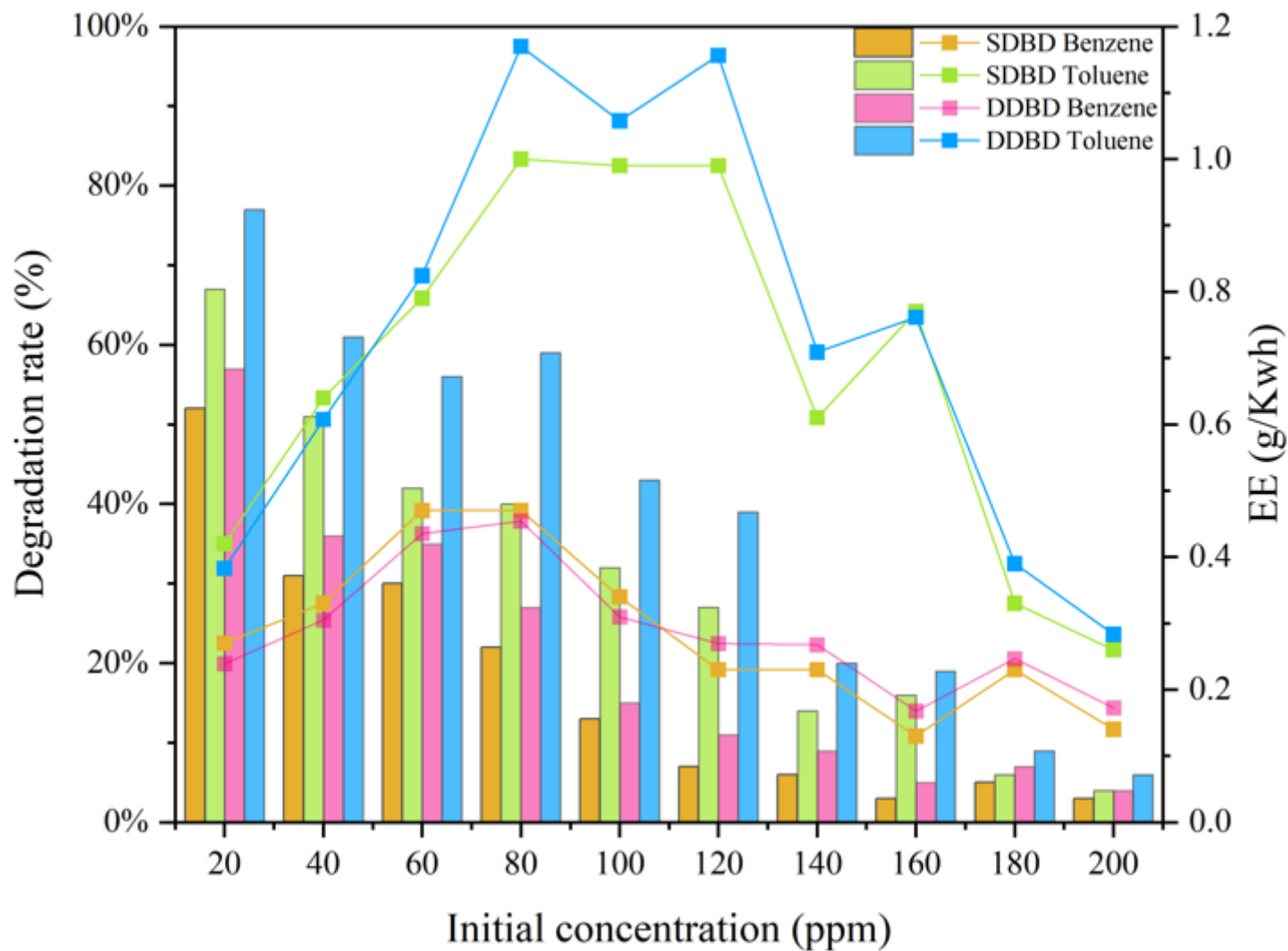


Figure 3

Relationship between benzene and toluene degradation rate, EE and Initial Concentration of SDBD and DDBD.

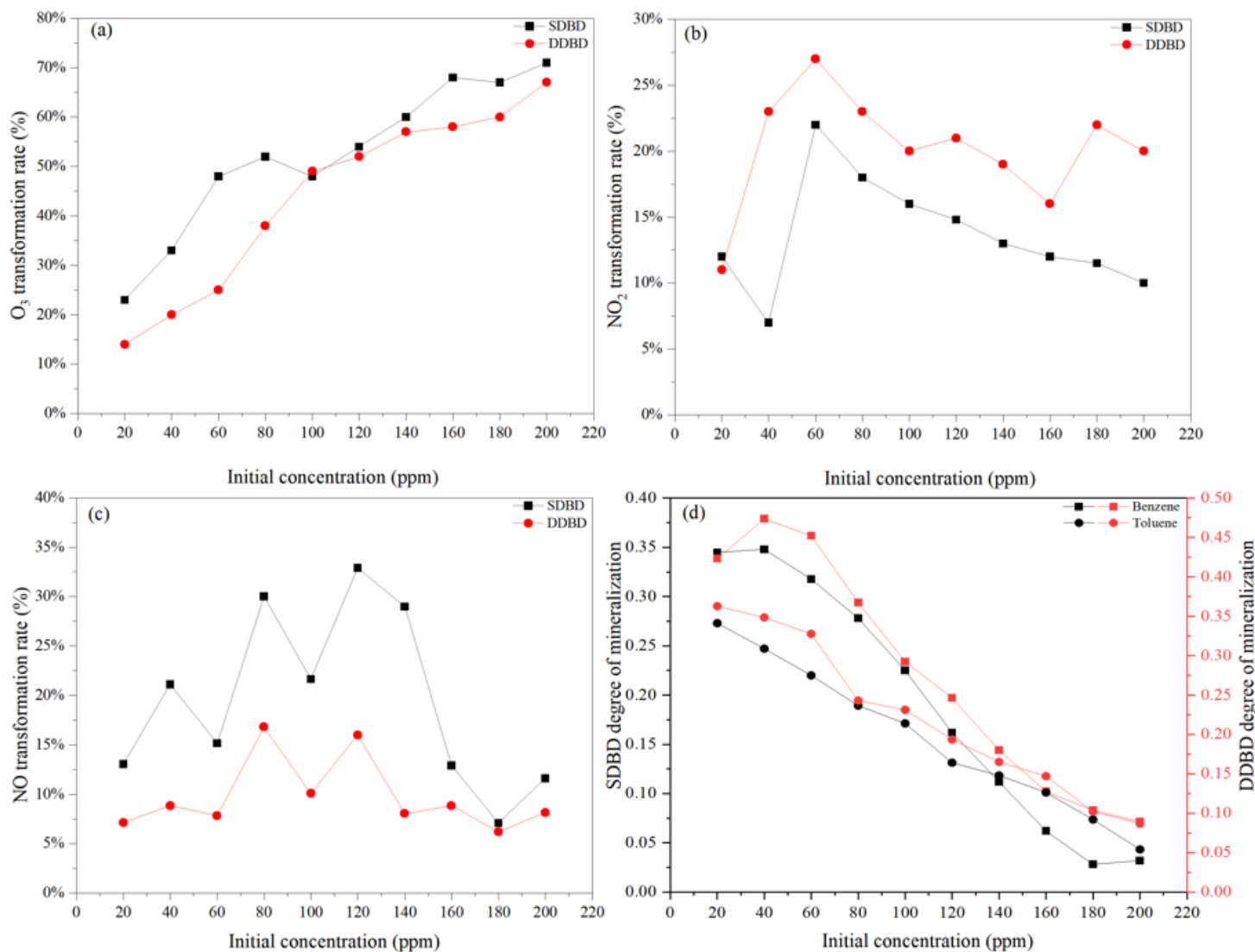


Figure 4

The relationship between by-product transformation, mineralization and initial concentration in SDBD and DDBD: (a) the relationship between different initial concentrations of SDBD and DDBD and O_3 transformation, (b) the relationship between different initial concentrations of SDBD and DDBD and NO_2 transformation, (c) the relationship between different initial concentrations of SDBD and DDBD and NO transformation, (d) the relationship between different initial concentrations of SDBD and DDBD and mineralization.

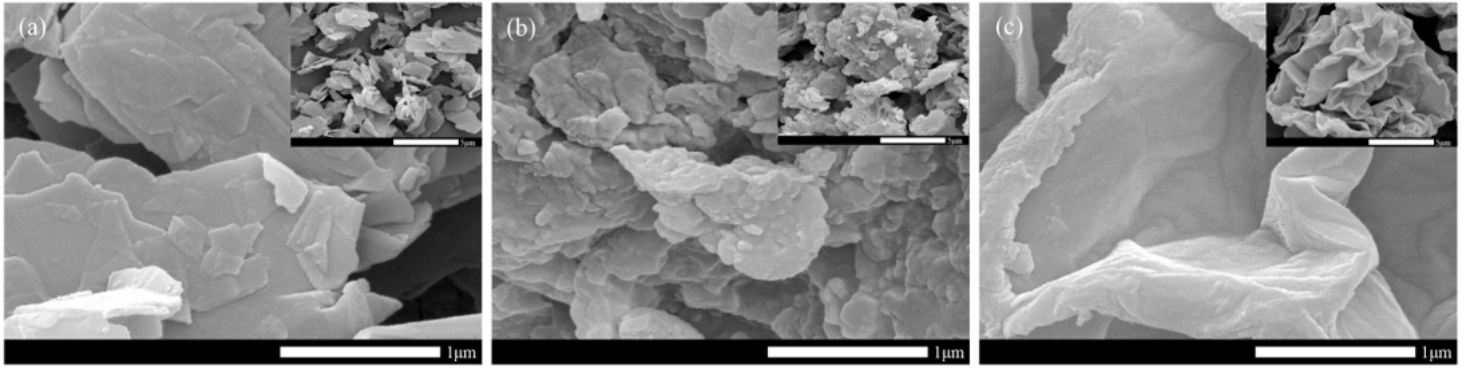


Figure 5

(a) SEM characterization of FG, (b) SEM characterization of GO1, (c) SEM characterization of GO2.

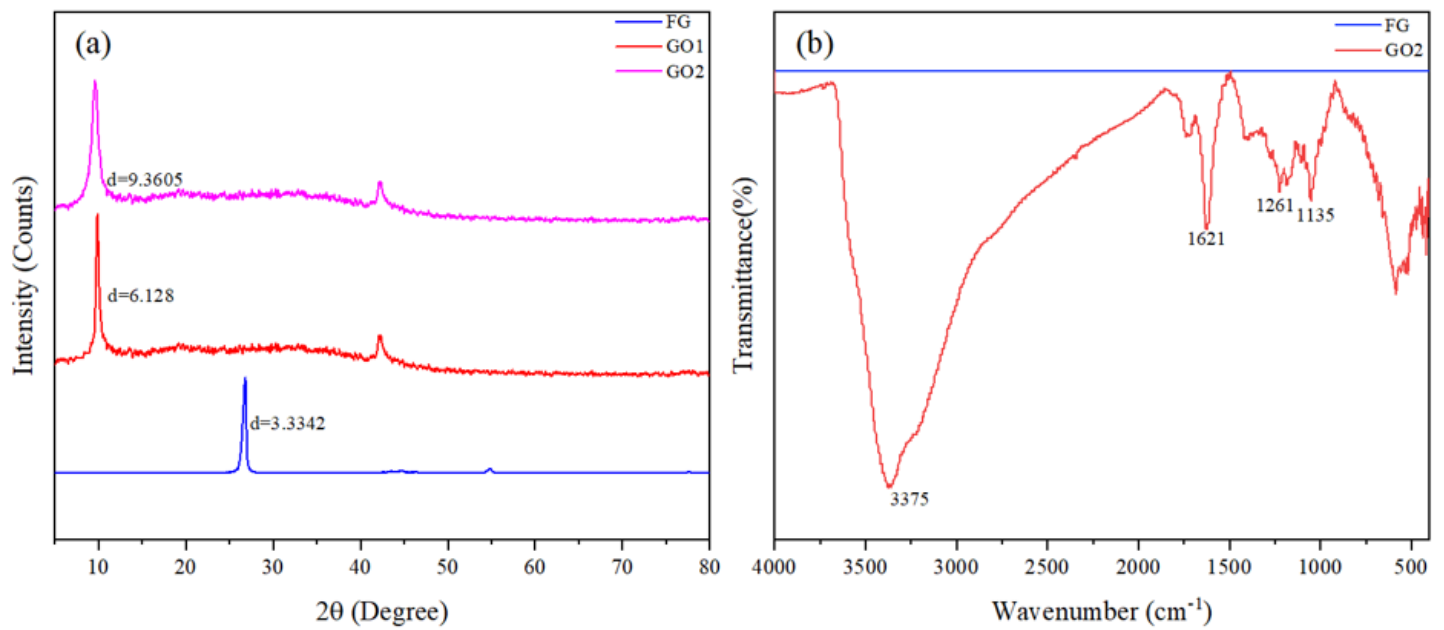


Figure 6

(a) XRD characterization of FG, GO1 and GO2, (b) FT-IR characterization of FG and GO2.

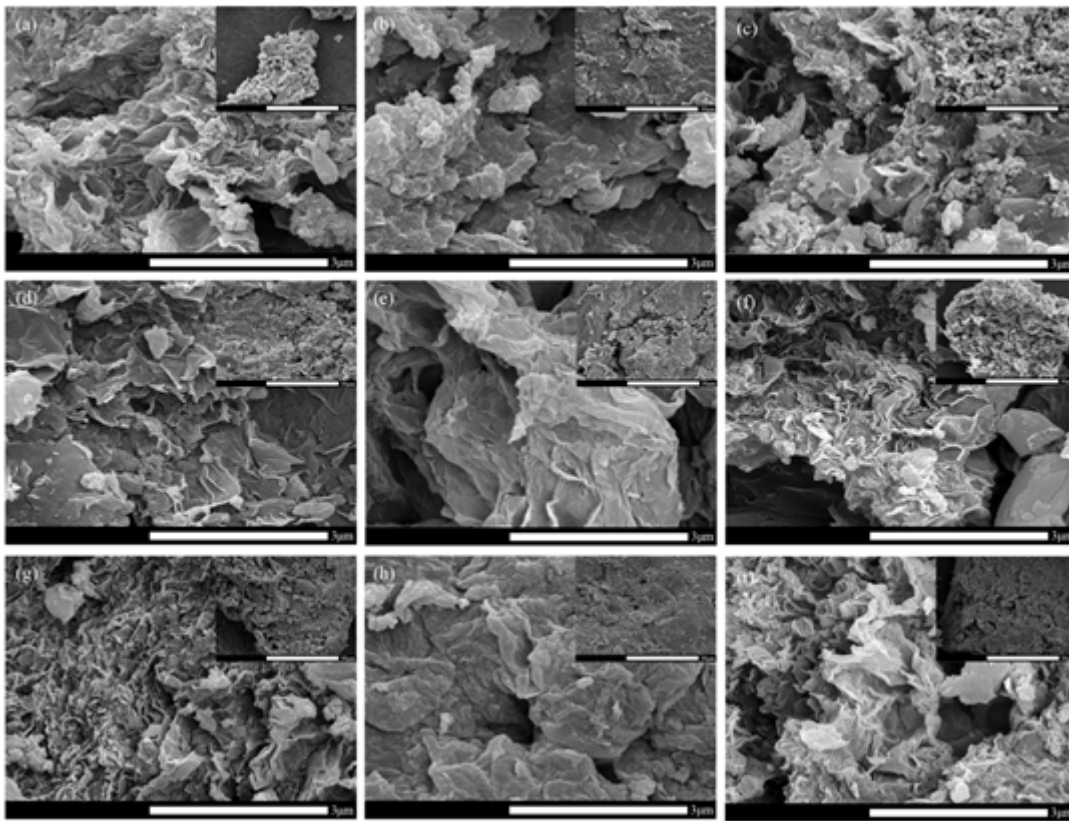


Figure 7

SEM characterization of different catalysts at different doses of [BMIM]PF₆: (a) SEM characterization of rGO/MnO_x at 0 ml of [BMIM]PF₆, (b) SEM characterization of rGO/MnO_x at 0.25 ml of [BMIM]PF₆, (c) SEM characterization of rGO/MnO_x at 0.5 ml of [BMIM]PF₆, (d) SEM characterization of rGO/FeO_x at 0 ml of [BMIM]PF₆, (e) SEM characterization of rGO/FeO_x at 0.25 ml of [BMIM]PF₆, (f) SEM characterization of rGO/FeO_x at 0.5 ml of [BMIM]PF₆, (g) SEM characterization of rGO/TiO_x at 0 ml of [BMIM]PF₆, (h) SEM characterization of rGO/TiO_x at 0.25 ml of [BMIM]PF₆, (i) SEM characterization of rGO/TiO_x at 0.5 ml of [BMIM]PF₆.

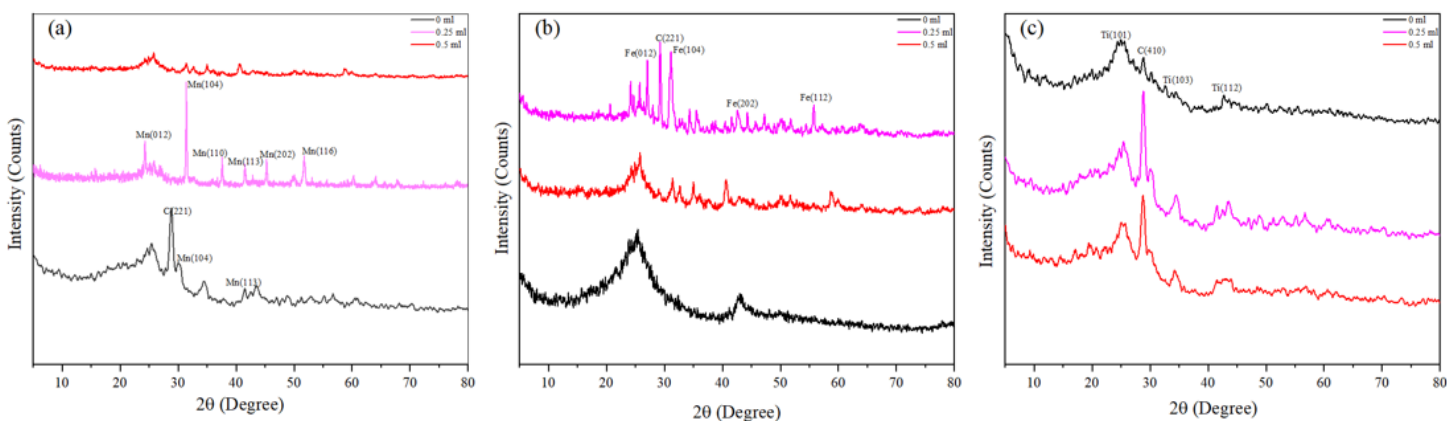


Figure 8

(a) XRD characterization of rGO/MnOx at different doses of [BMIM]PF6, (b) XRD characterization of rGO/FeOx at different doses of [BMIM]PF6, (c) XRD characterization of rGO/TiOx at different doses of [BMIM]PF6.

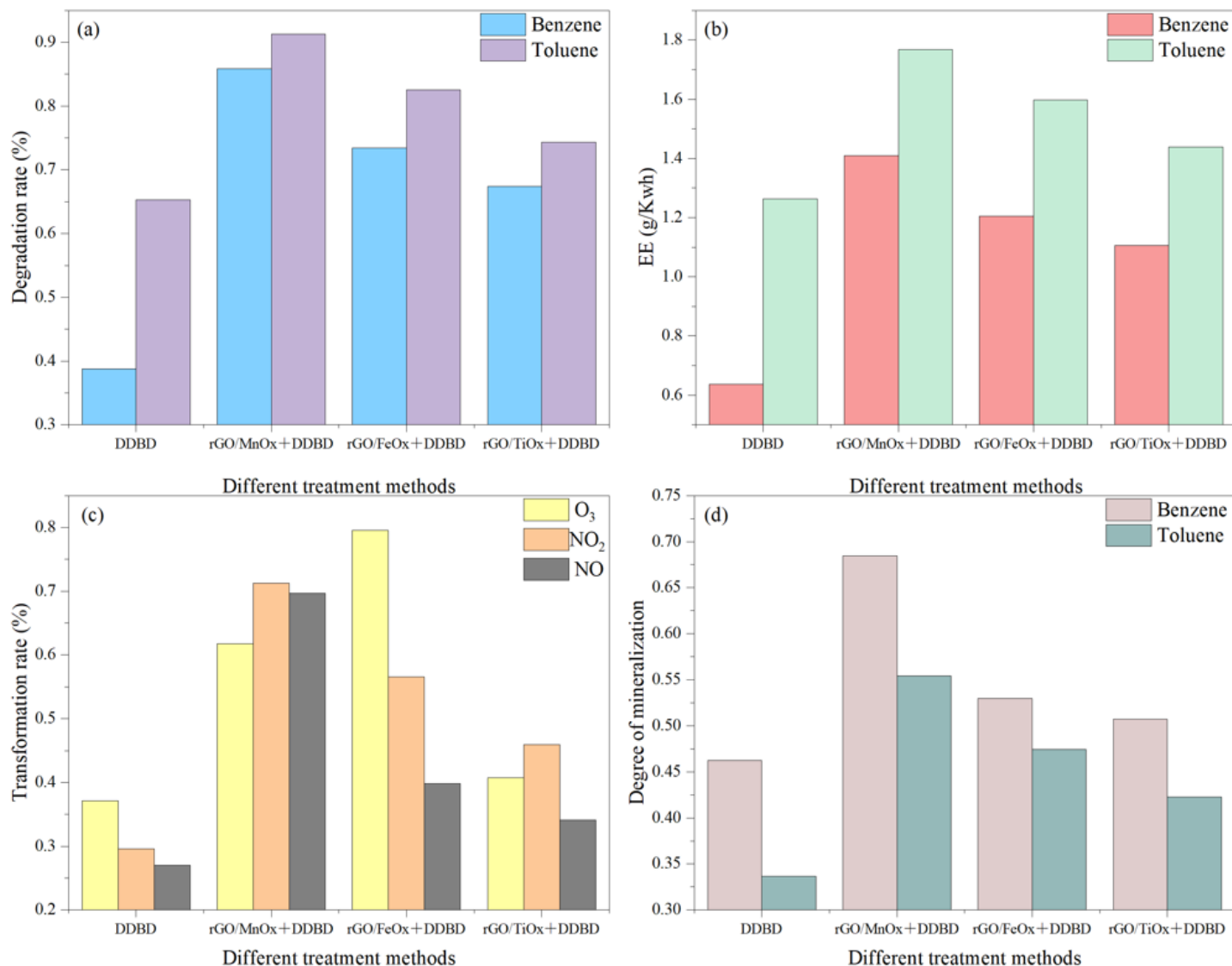


Figure 9

(a) Degradation rates of benzene and toluene by different treatment methods, (b) EE of different treatment methods in degradation of benzene and toluene, (c) The by-products transformation rate of different treatment methods, (d) The mineralization degrees of benzene and toluene degraded by different methods.

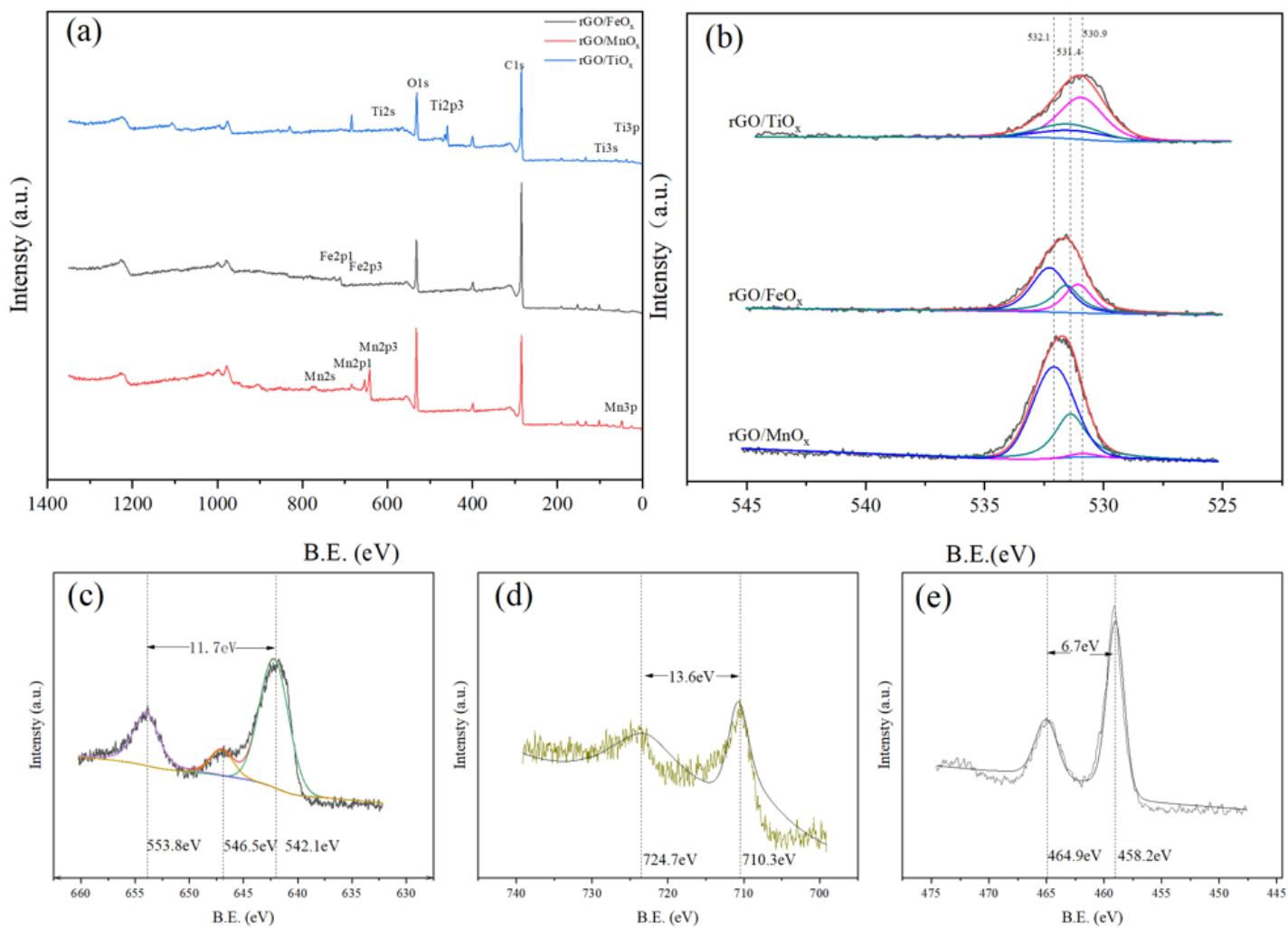


Figure 10

XPS full spectrum analysis of rGO/MnO_x, rGO/FeO_x and rGO/TiO_x, (b) O_{1s} analysis of rGO/MnO_x, rGO/FeO_x, rGO/TiO_x, (c) Mn_{2p} spectrum analysis of rGO/MnO_x, (d) Fe_{2p} spectrum analysis of rGO/FeO_x, (e) Ti_{2p} spectrum analysis of rGO/TiO_x.

Supplementary Files

This is a list of supplementary files associated with this preprint. Click to download.

- [Supplementarymaterials.docx](#)